ROYAL SOCIETY OF CHEMISTRY

PAPER

Check for updates

Near-infrared Cr^{3+}-doped lead-free halide perovskite microcrystals for information encryption and temperature thermometry†

Wei Zhao,[a] Li Li, ID *[a] Faling Ling, ID [a] Yongjie Wang, ID *[a] Guotao Xiang, ID [a] Xianju Zhou, ID [a] Sha Jiang,[a] Zhiyu Yang,[a] Yongbin Hua ID [b] and Jae Su Yu ID *[b]

Lead-free double perovskite materials have attracted lots of interest because they can be doped with luminescence activators to modify their optical characteristics and improve photoluminescence performances. Herein, a solvothermal method was utilized to synthesize single Cr^{3+}-doped $Cs_2NaInCl_6$ phosphors. Under 292 nm excitation, Cr^{3+}-doped $Cs_2NaInCl_6$ microparticles exhibited a strong broad near-infrared emission with a good photoluminescence quantum yield of 42.9%. The prepared sample exhibited a prominent peak at 960 nm and a full width at half maximum of 138 nm, which can be attributed to the spin-allowed transition ($^4T_2 \rightarrow {}^4A_2$) of Cr^{3+} ions. Additionally, the emission band of Cr^{3+} displayed a noticeable red shift as temperature increased owing to the variations in the strength of the crystal field. The thermometry based on the bandwidth and band-shift modes showed good sensitivities of 0.337 nm K^{-1} and 0.272 nm K^{-1}, respectively. Finally, the security ink was made for information encryption.

1. Introduction

Metal halide perovskites have exhibited remarkable potential for numerous applications, including solar cells,[1] light-emitting diodes,[2] photodetectors,[3] and more, owing to their exceptional optoelectronic properties.[4] $CsPbBr_3$ is a representative Pb-based perovskite that has garnered significant interest due to its high quantum yield.[5,6] However, the widespread commercialization of these substances has been impeded because of their instability and toxicity.[7] To address this, researchers have explored various strategies to replace lead with non-toxic or low-toxic elements.[8] Among these methods, using a monovalent metal cation (B^+) and a trivalent metal cation (B^{3+}) simultaneously for the heterovalent replacement of Pb^{2+} ions stands out as one of the most efficient approaches.[9,10] In this instance, the double perovskite is represented by $A_2B(I)B(II)X_6$ (A = Cs^+; B(I) = Ag^+, Na^+; B(II) = In^{3+}, Sb^{3+}, Bi^{3+}; X = Cl^-, Br^-) with a distinctive structure and superior performance, which can be distinguished by a three-dimensional framework consisting of vicissitudinary corner-sharing

octahedra $[B^+X_6]$ and $[B^{3+}X_6]$.[11,12] Although the optical properties of those lead-free metal halide perovskite hosts is significantly inferior to that of Pb-based materials, there are more methods to modify the composition and spectrum by involving ion doping and alloying.[13] Recently, $Cs_2NaInCl_6$ with excellent moisture, light, and thermal stabilities has attracted plenty of attention as one of the direct band gap double perovskites.[14] Zeng *et al.* incorporated Sb^{3+} ions into $Cs_2NaInCl_6$ to adjust the band structure for obtaining efficient blue light.[15] Nie *et al.* used Er^{3+} and Ho^{3+} ion co-doped $Cs_2NaInCl_6:Sb^{3+}$ to achieve adjustable white light emission.[16] As we know, the near-infrared (NIR) emission spectra of common rare earth activated ions Pr^{3+}, Nd^{3+}, Tm^{3+} and Yb^{3+} are too narrow, and the raw materials are expensive.[17] Therefore, incorporating Cr^{3+} ions into lead-free metal halide perovskites is a wise decision because they have the capability to generate a broad range of emissions, spanning from 650 to 1350 nm when situated within a crystal field of weak octahedral coordination.[18,19] Meanwhile, the selective capturing of invisible NIR light information encryption modes was expected to enable greater security levels and has widespread usage in daily life.

Temperature, as a fundamental physical quantity, plays an important role in our daily lives.[20] Therefore, temperature measurement technology has received significant attention and been developed.[21] Optical temperature measurement is a non-contact, fast, and accurate method for measuring temperature, which has plenty of applications in industries, healthcare,

[a] *School of Science, Chongqing University of Posts and Telecommunications, Chongqing, 400065, P. R. China. E-mail: lilic@cqupt.edu.cn, wangyj@cqupt.edu.cn*

[b] *Department of Electronics and Information Convergence Engineering, Institute for Wearable Convergence Electronics, Kyung Hee University, Yongin-si, Gyeonggi-do 17104, Republic of Korea. E-mail: jsyu@khu.ac.kr*

† Electronic supplementary information (ESI) available. See DOI: https://doi.org/10.1039/d3tc04453j

This journal is © The Royal Society of Chemistry 2024

J. Mater. Chem. C, 2024, **12**, 4627–4639 | **4627**

and environmental sectors, providing us with an efficient and convenient means of temperature monitoring.[22,23] The utilization of the luminescence intensity ratio (LIR) from the 4f–4f transitions of lanthanide elements is extensively employed as a widely adopted approach in optical temperature measurement for temperature sensing.[24,25] Lanthanide elements have unique optical properties, for instance, longer emission lifetimes and narrower absorption/emission lines.[26] However, the utilization of bandwidth (full width at half maximum (FWHM)) or spectral position (peak centroid) of emission bands for temperature sensing has been relatively limited in previous studies.[27] Possible reasons include the minor temperature-induced band shifts or FWHM variations for 4f–4f transitions.[28] To effectively overcome these limitations, a promising approach involves harnessing transition metal ions that demonstrate high sensitivity towards local coordination environments and consequently respond to the changes in lattice volume caused by variations in temperatures.[29]

In this study, we successfully synthesized a highly efficient phosphor that emits NIR light by incorporating Cr^{3+} ions into the $Cs_2NaInCl_6$ double perovskite structure using a convenient hydrothermal method. Using X-ray diffraction (XRD), the crystal structure of $Cs_2NaInCl_6$:Cr^{3+} double perovskite was determined, while morphological characterization was conducted by scanning electron microscopy (SEM) analysis. Additionally, X-ray photoelectron spectroscopy (XPS) and electron paramagnetic resonance (EPR) were performed to further analyze the electronic and crystal structures. The $Cs_2NaInCl_6$:Cr^{3+} double perovskite exhibited broadband NIR emission (λ_{em} = 960 nm, FWHM = 138 nm) under 292 nm excitation. Eventually, this material showcased its potential in NIR information encryption and optical temperature measurement in this work.

2. Experimental section

2.1 Materials

CsCl (99.9%, Aladdin), NaCl (99.9%, Aladdin), $InCl_3$ (99.9%, Aladdin), $CrCl_3·6H_2O$ (analytical pure, Chengdu Kelong Chemical Reagent Factory, China), hydrochloric acid (HCl, 37%, Chongqing Chuandong Chemical, China), and ethanol (analytical pure, Chongqing Chuandong Chemical, China) were used. The chemicals are procured commercially and employed without undergoing additional purification.

2.2 Synthesis of $Cs_2NaInCl_6$:xCr^{3+} phosphors

$Cs_2NaInCl_6$:xCr^{3+} (x = 0, 0.03, 0.06, 0.09, 0.12, and 0.15) phosphors were synthesized *via* the solvothermal method. 2 mmol CsCl, 1 mmol NaCl, $1 - x$ mmol $InCl_3$, and x mmol $CrCl_3·6H_2O$ were dissolved in 12.5 mL of hydrochloric acid and then transferred into a 50 mL Teflon autoclave. The solution was heated at 180 °C for 12 h and then cooled to room temperature at a slow and consistent speed. Finally, the microcrystals were collected, washed multiple times with ethanol, and dried overnight in a vacuum furnace.

2.3 Characterization

The utilized powders were all obtained by grinding in a mortar. The powder samples were subjected to the XRD (Cu Kα radiation λ = 1.54 Å) measurements at a constant scanning rate of 2° min⁻¹. The Rietveld refinement was carried out with the assistance of the universal structure analysis system (Fullprof) program. The morphology and energy dispersive X-ray spectroscopy (EDS) analyses of the as-synthesized phosphor were performed by SEM. The XPS was performed by Thermo Scientific K-Alpha. The EPR measurements were carried out by using a conventional Bruker EMX PLUS spectrometer.
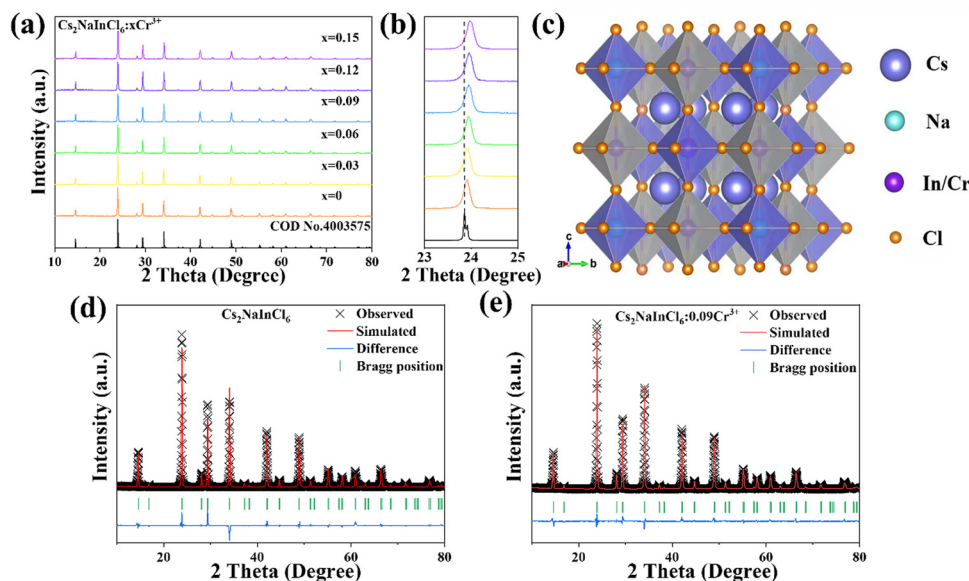

Fig. 1 (a) XRD patterns and (b) selected diffraction peaks at around 24° of the as-prepared $Cs_2NaInCl_6$:xCr^{3+} (x = 0, 0.03, 0.06, 0.09, 0.12, and 0.15). (c) Schematic illustration of the crystal structure of $Cs_2NaInCl_6$:Cr^{3+} double perovskite. Rietveld refinement results of (d) the $Cs_2NaInCl_6$ host and (e) the $Cs_2NaInCl_6$:$0.09Cr^{3+}$ sample.

4628 | *J. Mater. Chem. C*, 2024, **12**, 4627–4639

This journal is © The Royal Society of Chemistry 2024

Table 1 Refinements results of $Cs_2NaInCl_6:xCr^{3+}$ (x = 0 and 0.09)

Parameters	$Cs_2NaInCl_6$	$Cs_2NaInCl_6:0.09Cr^{3+}$
Radiation type λ (Å)	X-ray, 1.5406	X-ray, 1.5406
2 theta range (degree)	10–80	10–80
Space group	$Fm\bar{3}m$	$Fm\bar{3}m$
Crystal system	Cubic	Cubic
$a = b = c$ (Å)	10.53103	10.52582
Volume (Å³)	1167.917	1166.186
$\alpha = \gamma = \beta$ (°)	90.0000	90.0000
R_{wp}	12.0%	10.2%
R_p	9.23%	7.37%
χ^2	4.27	3.17

Ultraviolet-visible (UV-Vis) absorbance spectroscopy was carried out on a Agilent Carry 5000 spectrophotometer supplied with an integrating sphere. In addition, the photoluminescence excitation (PLE) spectra, photoluminescence (PL) emission spectra, PL quantum yield (PLQY), and decay lifetime were measured using a FLS1000 fluorescence spectrophotometer (Edinburgh Instruments Ltd, UK). Thermogravimetric analysis (TGA) was performed through a Thermogravimetric Analyzer TGA STD Q600. Meanwhile, a standard Nikon Z30 camera and a NIR camera (Basler a2A1280-125μm) were employed to acquire visible and NIR images correspondingly.

2.4 Computational method

We utilized density functional theory (DFT) to perform preliminary calculations.[30] To account for the exchange–correlation effects among electrons, we utilized the generalized gradient
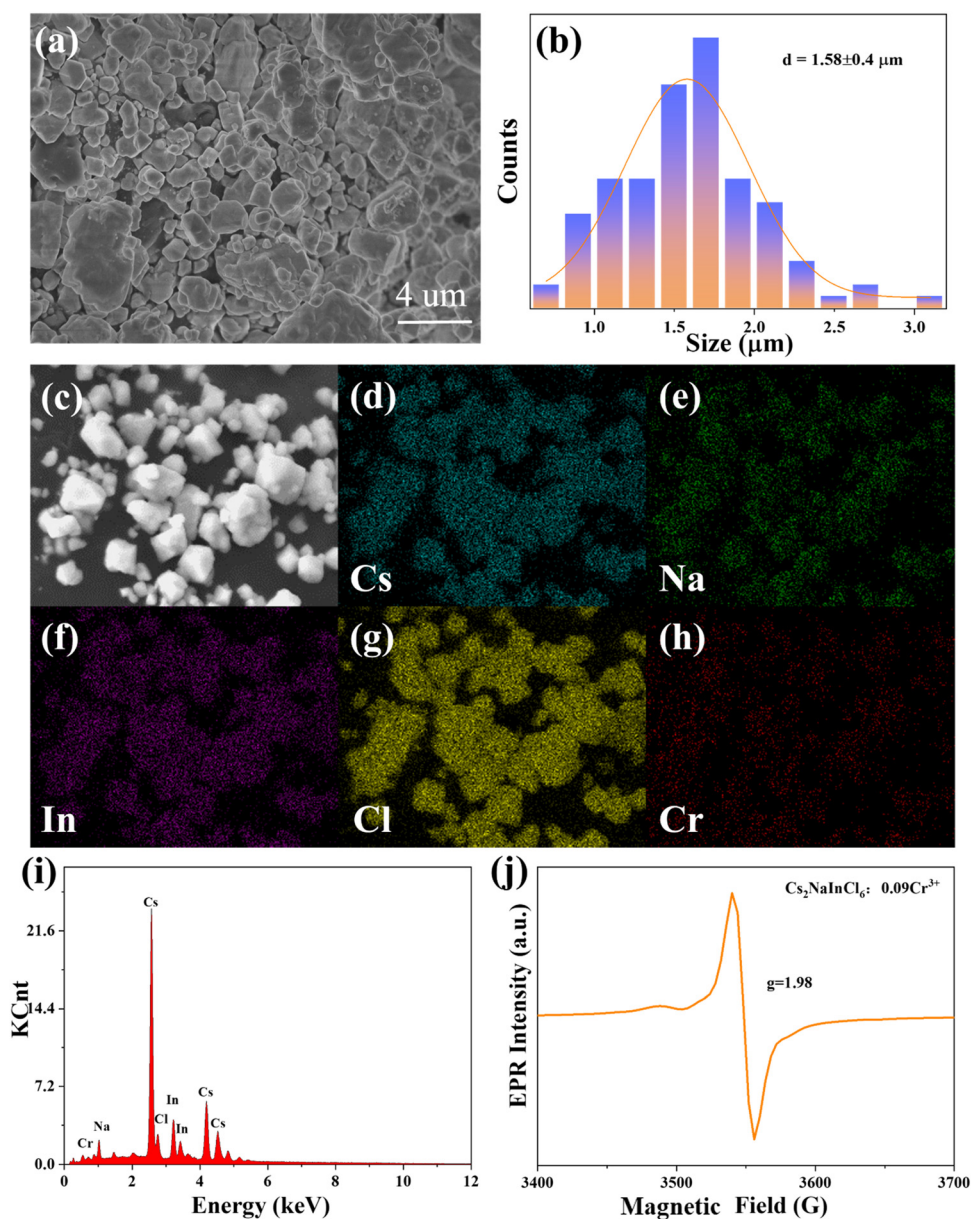

Fig. 2 (a) SEM image and (b) corresponding size distribution histograms of $Cs_2NaInCl_6:0.09Cr^{3+}$. (c)–(h) Layered electronic image and elemental mapping images of the $Cs_2NaInCl_6:0.09Cr^{3+}$ sample. (i) EDS spectrum and (j) EPR spectrum for the $Cs_2NaInCl_6:0.09Cr^{3+}$ phosphor.

approximation (GGA-PBE).[31] A plane wave cut-off energy of 500 eV was employed for both structural optimizations and electronic calculations. The Monkhorst–Pack scheme was utilized to generate k-point meshes for various structures within the Brillouin zones, with a size of $12 \times 12 \times 12$ for primitive $Cs_2NaInCl_6$.

3. Results and discussion

The XRD patterns of the prepared $Cs_2NaInCl_6$:xCr^{3+} (x = 0, 0.03, 0.06, 0.09, 0.12, and 0.15) samples are depicted in Fig. 1a. There are no observable additional diffraction peaks present in any of the samples, demonstrating that the doping of Cr^{3+} ions has no significant influence on the crystal structure of $Cs_2NaInCl_6$. Simultaneously, it is found that the characteristic diffraction peak (220) alters monotonically to a higher angle with an increase in the Cr^{3+} ion concentration (Fig. 1b). According to the known Bragg theory, Cr^{3+} (0.615 Å, CN = 6) with a smaller ionic radius replaces In^{3+} (r = 0.81 Å, CN = 6) with a larger ionic radius, resulting in the reduction of cell volume. Meanwhile, according to previous reports, it is suggested that the Cr^{3+} ion takes up the In^{3+} sites, which balances the charge and follows the rule of matching ionic radii.[32] Therefore, the crystal structure diagram of $Cs_2NaInCl_6$:xCr^{3+} is shown in Fig. 1c, illustrating the face-centered cubic space group ($Fm\bar{3}m$) consisting of corner-connected octahedra [NaCl$_6$] and [InCl$_6$], with Cs$^+$ occupying the outside spaces, which results in a three-dimensional structure. The Rietveld XRD refinements were conducted using the structural data for COD no. 4003575 as an original model for analyzing the cell parameters of the prepared samples, as illustrated in Fig. 1d and e. The excellent quality of refinement results (R_{wp} < 15%, R_p < 10%) revealed the single-phase structure of the as-prepared materials, as shown in Table 1.

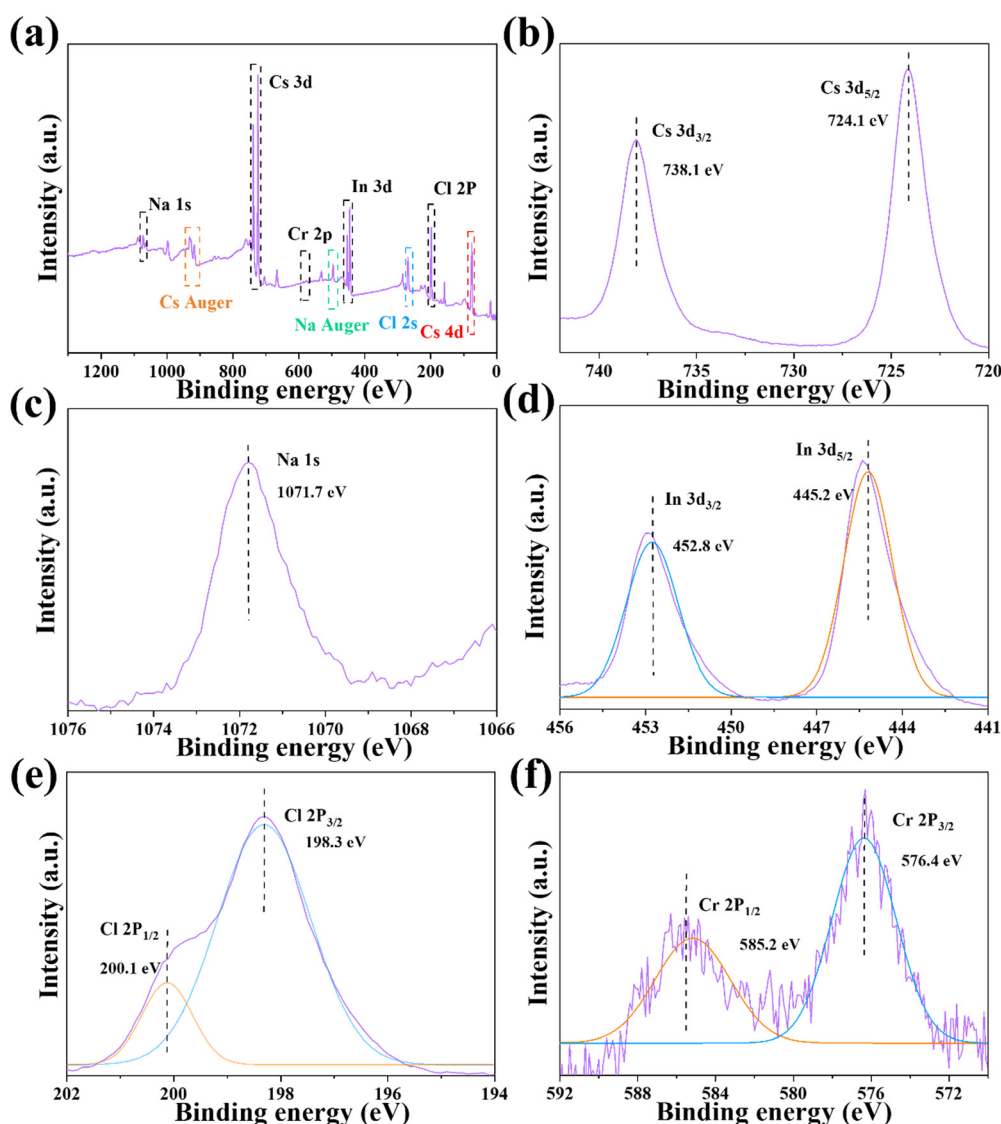**Fig. 3** (a) XPS core-level spectra of the (b) Cs$^+$ 3d, (c) Na$^+$ 1s, (d) In^{3+} 3d, (e) Cl$^-$ 2p, and (f) Cr^{3+} 2p for the $Cs_2NaInCl_6$:0.09Cr^{3+} phosphor.

Additionally, the decrease in cell volume from 1167.917 to 1166.186 Å^3 demonstrates that Cr^{3+} ions have been successfully acquired into the positions of In^{3+} ions.

The morphology of the $Cs_2NaInCl_6{:}0.09Cr^{3+}$ sample, which exhibited an irregular form with an average diameter of 1.58 ± 0.4 μm, is displayed in Fig. 2a and b. The Cs, Na, In, Cl, and Cr were uniformly dispersed over the surface of the sample, as portrayed in Fig. 2c–h. Moreover, Fig. 2i shows the EDS spectrum of the $Cs_2NaInCl_6{:}0.09Cr^{3+}$ phosphor, revealing the existence of Cs, Na, In, Cl, and Cr peaks. The chemical environment of the oxidation state of the Cr ion in the host can be studied by EPR spectroscopy. The EPR spectrum of $Cs_2NaInCl_6{:}0.09Cr^{3+}$ is presented in Fig. 2j, and the coupling pattern structure with a distinctive g-factor of 1.98 may demonstrate the presence of Cr^{3+} ions.[33]

The XPS analysis was conducted to further investigate the electronic properties and elemental construction of $Cs_2NaInCl_6{:}0.09Cr^{3+}$. The obtained results confirmed the presence of all the basic elements in $Cs_2NaInCl_6{:}0.09Cr^{3+}$ as illustrated in Fig. 3a–e. Specifically, the Cs 3d peak exhibited two components at the states of $3d_{3/2}$ (738.1 eV) and $3d_{5/2}$ (724.1 eV).[34]

Similarly, the In 3d core level exhibited two peaks at the binding energy at 452.8 and 445.2 eV, as specified to the states of In^{3+} $3d_{3/2}$ and $3d_{5/2}$.[35] A peak at 1071.7 eV was assigned to Na 1s.[36] The Cr 2p spectrum exhibited two separate peaks at 585.2 and 576.4 eV, corresponding to the orbitals of Cr^{3+} ions at the states of $2p_{1/2}$ and $2p_{3/2}$, respectively. The observed binding energy of the Cr 2p electrons was consistent with previous research conducted on octahedral Cr^{3+} ions.[37] The above results clearly verify the successful preparation of $Cs_2NaInCl_6{:}Cr^{3+}$ phosphors.

The pristine and Cr^{3+} substituted compounds were analyzed for their electronic band structures using DFT simulation. Fig. 4a and b display the electronic band structures of $Cs_2NaInCl_6$. The $Cs_2NaInCl_6$ exhibits a direct electronic transition with the calculated band gap (E_g) of 3.04 eV, which is approximately equal to the previously calculated result (E_g = 2.96 eV).[38] The Cl 3p orbitals are the primary origin of the valence band maximum, while the conduction band minimum was predominantly contributed by both the Cl 3p and In 5s orbitals. From the band structures of $Cs_2NaInCl_6{:}Cr^{3+}$ as illustrated in Fig. 4c, the band gap for $Cs_2NaInCl_6$ host decreases
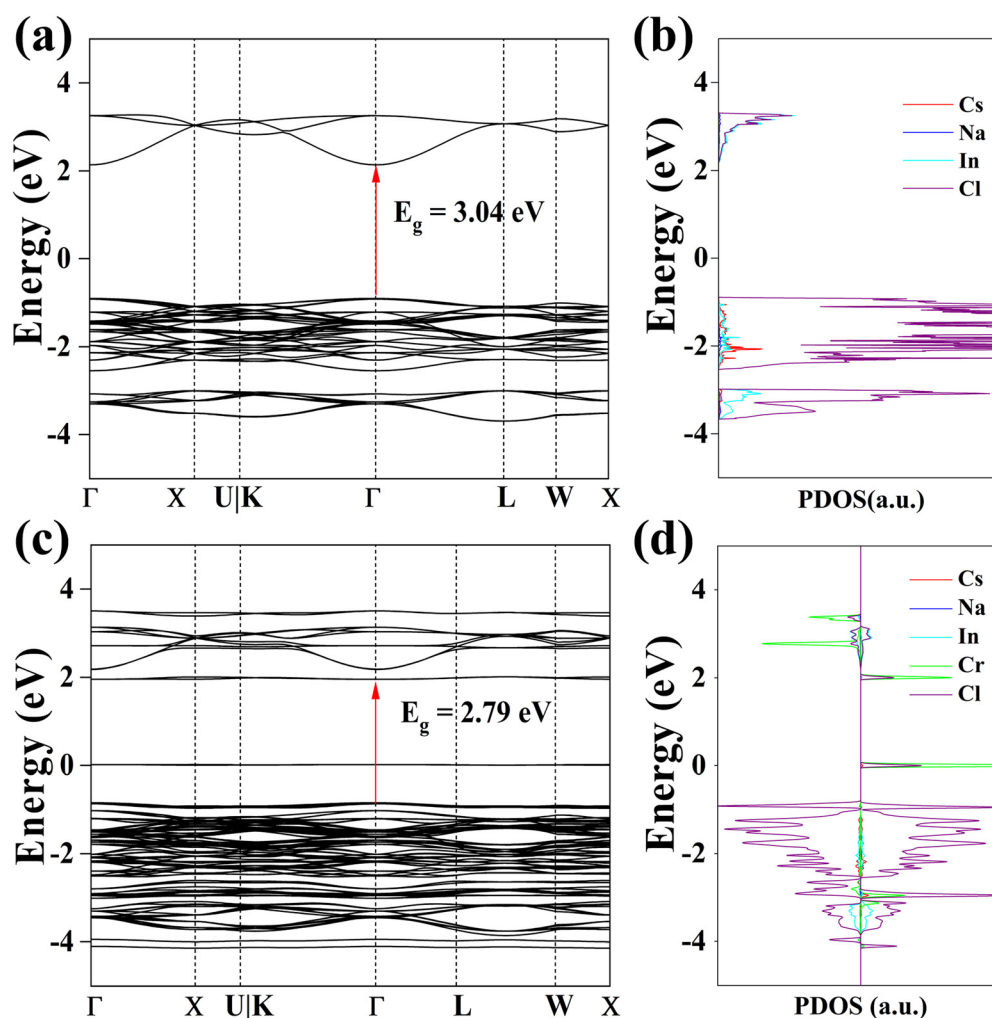

Fig. 4 (a) Calculated band structure and (b) density of state of $Cs_2NaInCl_6$ host. (c) Calculated band structure and (d) density of state of $Cs_2NaInCl_6{:}Cr^{3+}$.
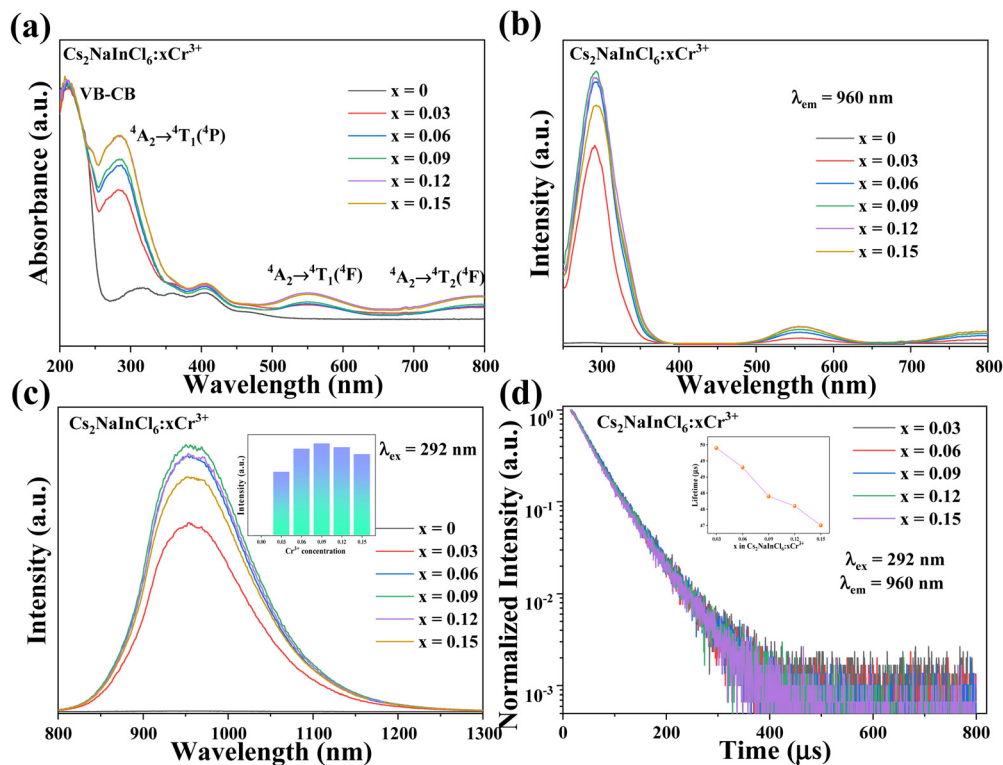
Fig. 5 (a) UV-Vis absorbance spectra. (b) PLE and (c) PL spectra of $Cs_2NaInCl_6:Cr^{3+}$ with different Cr^{3+} ion concentrations. Inset of (c) shows the corresponding PL intensity. (d) Luminescence decay curves of the $Cs_2NaInCl_6:Cr^{3+}$ samples measured at room temperature.

from 3.04 to 2.79 eV. Meanwhile, we observe the formation of Cr 3d states in the proximity of the Fermi energy (Fig. 4d). The band gap change may be associated with a modification in strength as well as the nature of the host crystal and the effect of the energy level of doping ions.[39] Even though it is semi-qualitative in nature, the interpretation at the DFT level of theory provides crucial details on the placement of the chrome ion orbitals in the host band gap and provides insights into the performance of this material as a phosphor.

The PL properties of the synthesized products were subsequently investigated. Fig. 5a displays the UV-Vis absorption spectra of all the $Cs_2NaInCl_6:xCr^{3+}$ ($x = 0$, 0.03, 0.06, 0.09, 0.12, and 0.15) samples. It is unambiguous from the absorption spectra that there is a peak apparent at around 221 nm, which belongs to the electron transitions from the host valence band to its conduction band. Meanwhile, the absorption bands at 285, 552, and 795 nm could be credited to the d–d transitions of $^4A_2 \rightarrow {}^4T_1(^4P)$, $^4A_2 \rightarrow {}^4T_1(^4F)$ and $^4A_2 \rightarrow {}^4T_2(^4F)$ of Cr^{3+} ions.[40] Furthermore, Fig. 5b shows the PLE spectra of $Cs_2NaInCl_6:xCr^{3+}$. There are three excitation peaks that could be well matched to the Cr^{3+} absorption bands of the UV-Vis absorption under the emission wavelength of 960 nm. Specifically, these three bands were in the violet (about 292 nm), green (around 558 nm), and deep red (around 797 nm) regions. The correlation between concentration of Cr^{3+} ions and the intensity of PL emission is presented in Fig. 5b and c. The PL emission intensity exhibits an increased tendency with the increment of Cr^{3+} ion concentration and the maximum intensity was

Table 2 Comparison of $\lambda_{ex}/\lambda_{em}$, FWHM, Dq/B, and PLQY of $Cs_2NaInCl_6:Cr^{3+}$ with previously reported Cr^{3+}-activated broadband NIR phosphors

Sample	$\lambda_{ex}/\lambda_{em}$ (nm)	FWHM (nm)	Dq/B	PLQY (%)	Ref.
$Sr_2InSbO_6:Cr^{3+}$	558/955	—	1.96	14.5	18
$Cs_2AgInCl_6:Cr^{3+}/Yb^{3+}$	365/1000	188	2.25	45.0	34
$Cs_2AgInCl_6:Cr^{3+}$	353/1010	180	—	22.0	50
$Ca_2InTaO_6:Cr^{3+}$	440/880	200	2.26	33.6	55
$NaGaP_2O_7:Cr^{3+}$	460/793	115	1.98	56.4	56
$KGaP_2O_7:Cr^{3+}$	460/815	127	1.96	74.7	57
$Sr_9Ga(PO_4)_7:Cr^{3+}$	485/850	140	—	66.3	58
$Cs_2NaInCl_6:Cr^{3+}$	292/960	138	2.28	42.9	This work

obtained at $x = 0.09$. At this concentration, the PL spectrum exhibited strong NIR emission centered at 960 nm with the FWHM of 138 nm assigned to the spin-allowed $^4T_2 \rightarrow {}^4A_2$ transition of octahedrally coordinated Cr^{3+} ions.[41,42] Meanwhile, the PL emission spectra do not exhibit noticeable alteration, which suggests that there is no effect of the Cr^{3+} ion concentration on the crystal field environment.[43] Additionally, Fig. S1 (ESI†) illustrates a measured PLQY value of approximately 42.9% for $Cs_2NaInCl_6:0.09Cr^{3+}$. By comparing some recent reports (Table 2), it is reasonable to consider that the obtained samples may be suitable for some optical applications.

The decay curves of $Cs_2NaInCl_6:xCr^{3+}$ were measured at 960 nm emission wavelength and 292 nm excitation wavelength (Fig. 5d). Furthermore, the average lifetime could be calculated
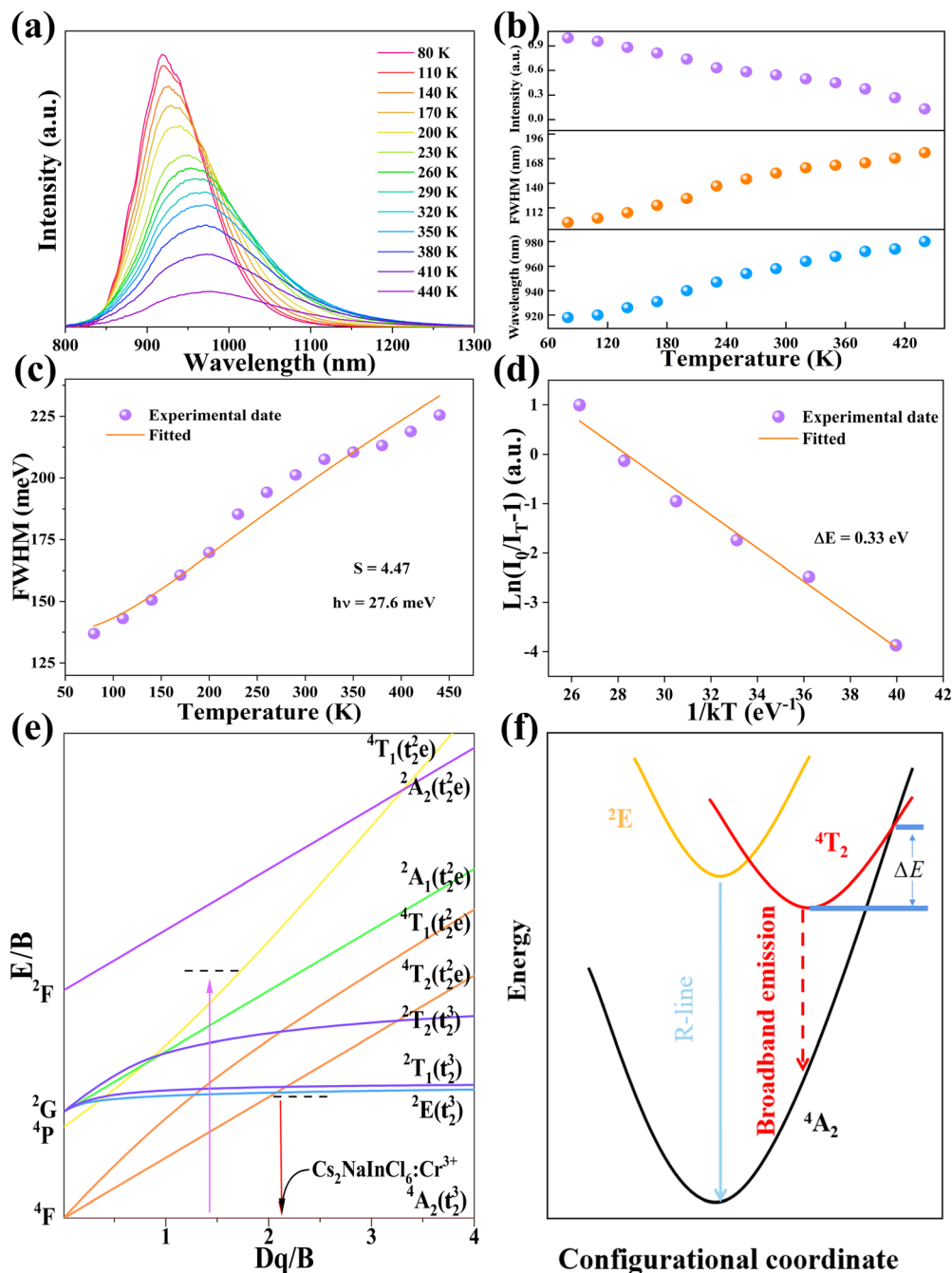
4632 | *J. Mater. Chem. C*, 2024, **12**, 4627–4639

This journal is © The Royal Society of Chemistry 2024

Fig. 6 (a) Temperature-dependent PL emission spectra of $Cs_2NaInCl_6$:0.09Cr^{3+}. (b) Temperature-dependent PL intensity, FWHM, and peak wavelength of $Cs_2NaInCl_6$:0.09Cr^{3+}. (c) Fitting of the FWHM as a function of temperature. (d) Fitting Arrhenius equation for thermal quenching. (e) Tanabe–Sugano energy level diagram of Cr^{3+} in an octahedral crystal field. (f) Diagram of Cr^{3+} configurational coordinates in a weak crystal field.

using the following eqn (1) and (2):[44]

$$I(t) = I_0 + A_1 \exp\left(-\frac{t}{\tau_1}\right) + A_2 \exp\left(-\frac{t}{\tau_2}\right) \quad (1)$$

$$\tau_{ave} = (A_1\tau_1{}^2 + A_2\tau_2{}^2)/(A_1\tau_1 + A_2\tau_2) \quad (2)$$

Here, the intensity at time t and $t = 0$ is denoted as $I(t)$ and I_0, respectively, and A_1 and A_2 are constants. τ_1 and τ_2 are the

components of lifespan, and τ_{ave} represents the average decay lifetime. The lifetime values of $Cs_2NaInCl_6$:$x$$Cr^{3+}$ (x = 0.03, 0.06, 0.09, 0.12, and 0.15) were calculated to be 49.4, 48.8, 47.9, 47.6, and 47.0 μs, respectively. The decrease in the decay lifetime is attributable to the increased occurrence of non-radiative transitions when the Cr^{3+} ion concentration is elevated.[45]

Temperature-dependent PL spectra of $Cs_2NaInCl_6$:0.09 Cr^{3+} are seen in Fig. 6a. It is visible that different temperatures result in the measurement of a wide emission band

This journal is © The Royal Society of Chemistry 2024

J. Mater. Chem. C, 2024, 12, 4627–4639 | 4633

corresponding to the $^4T_2 \rightarrow {}^4A_2$ spin-allowed transition of Cr^{3+} ions. The peak wavelength of PL spectra was red-shifted as the temperature was raised from 80 to 440 K, but the PL emission intensity was declined and the FWHM of the PL spectra was increased from 95 to 183 nm (Fig. 6b). Typically, by finding the relationship between FWHM and temperature, the coupling effect between electrons and phonons can be defined using eqn (3):[46]

$$\text{FWHM} = 2.36\sqrt{S}h\nu\sqrt{\coth\frac{h\nu}{2kT}} \quad (3)$$

where $h\nu$ denotes the phonon frequency, T is the Kelvin temperature, S is the Huang–Rhys parameter, and k (8.629×10^{-5} eV) is the Boltzmann constant. The above model was used to fit the collected data (Fig. 6c). S was equal to 4.47 and $h\nu$ was calculated to be 27.6 meV. Generally, stronger electron–phonon coupling can result in a wider emission band of Cr^{3+} ions, but it often leads to more severe luminescence thermal quenching.[47] The activation energy (ΔE) can be calculated to further assess the thermal quenching mechanism based on eqn (4):[48]

$$I(T) = \frac{I_0}{1 + A \exp\left(\frac{-\Delta E}{kT}\right)} \quad (4)$$

where I_0 represents the initial emission intensity, $I(T)$ refers to the emission intensity at temperature T, A is a constant,

k stands for the Boltzmann's constant, and ΔE is the activation energy. Fig. 6d illustrates the fitting equation for thermal quenching, with an estimated activation energy of 0.33 eV.

The PL characteristics of the Cr^{3+} ions are highly dependent on the crystal environment because they have the $3d^3$ configuration, in which the 3d electrons are not protected from their surroundings by outer-filled shells. Due to the lower crystal field stabilization energy of an octahedron compared to a tetrahedron in coordination, the Cr^{3+} ion prefers to occupy one in a crystal material.[49] When Cr^{3+} ions are positioned in the core of coordinated octahedra, the effect of the host lattice on the luminescence properties of Cr^{3+} ions may be represented by the parameters of Dq and B, which are ascertained by using the subsequent eqn (5)–(7):[49]

$$10Dq = E\left({}^4T_2\right) = E\left({}^4A_2 \rightarrow {}^4T_2\right) \quad (5)$$

$$\frac{Dq}{B} = \frac{15(x-8)}{x^2 - 10x} \quad (6)$$

$$x = \frac{E\left({}^4T_1\right) - E\left({}^4T_2\right)}{Dq} = \frac{E\left({}^4A_2 \rightarrow {}^4T_1\right) - E\left({}^4A_2 \rightarrow {}^4T_2\right)}{Dq} \quad (7)$$

where Dq is the intensity of the crystal field and B is the Racah parameter. The value of x is derived from the energy variations between the $^4T_1(^4F)$ and $^4T_2(^4F)$ transitions gained from the PLE

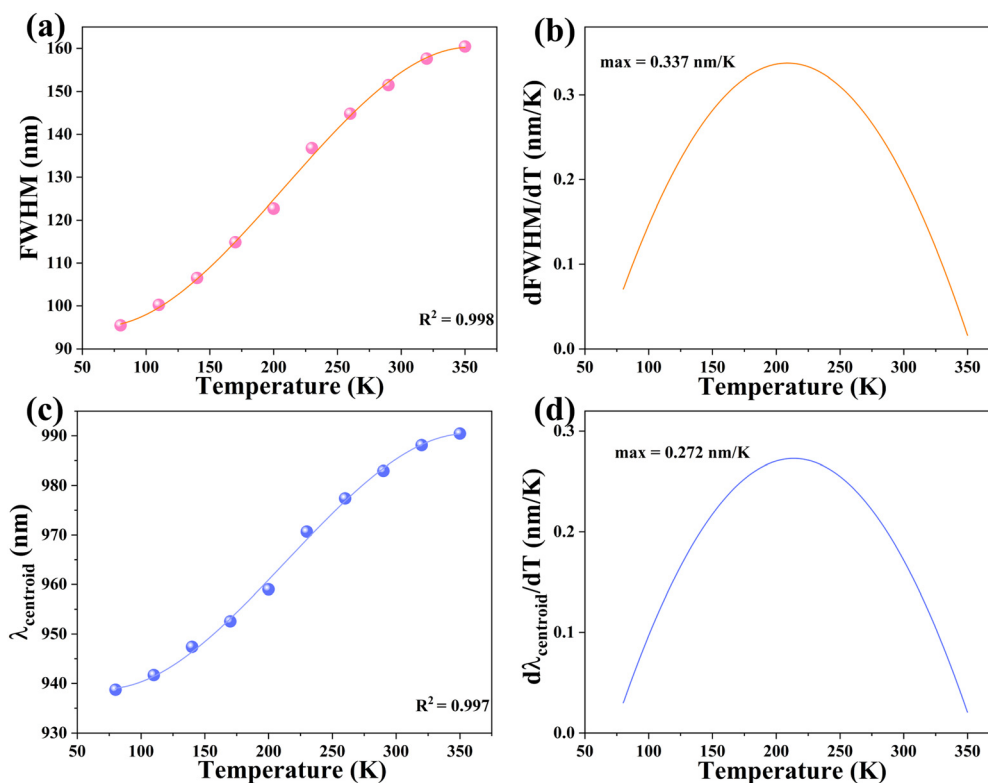**Fig. 7** (a) FWHM emission band and (b) sensitivity as a function of temperature for the $Cs_2NaInCl_6$:0.09Cr^{3+}. (c) Band centroid emission band and (d) sensitivity as a function of temperature for the $Cs_2NaInCl_6$:0.09Cr^{3+}.

4634 | *J. Mater. Chem. C*, 2024, **12**, 4627–4639

This journal is © The Royal Society of Chemistry 2024

spectra. The crystal field parameters, Dq and B, are predicted to be 1254.7 cm^{-1} and 550.5 cm^{-1}, respectively. Eventually, Dq/B was calculated as 2.28 for Cs$_2$NaInCl$_6$:Cr^{3+}, which is consistent with the $^4T_2 \rightarrow {}^4A_2$ transition related in the weak crystal field ($Dq/B < 2.3$) (Fig. 6e). The luminescence behavior may also be explained using the configurational coordinate model. Under the excitation of UV radiation, electrons are excited to the excited state from the ground state, as seen in Fig. 6f. The majority of electrons at room temperature return to the ground state *via* radiation. However, when the temperature increases, more electrons return to the ground state along the path of non-radiation from the crossing point. The PL intensity decreases as the temperature rises because more energy is lost through non-radiative transfer.[48] In this work, when the temperature increased from 80 to 440 K for the Cs$_2$NaInCl$_6$:Cr^{3+} phosphors, the dominant emission line of the NIR emission moved from 918 to 976 nm, because the crystal lattice grew and the lattice vibration became stronger as the temperature increased, resulting in the weak crystal field.[50] According to the Tanabe–Sugano energy level diagram for Cr^{3+} ions in the

octahedral symmetry, the crystal field weakens, causing the emission spectra to red shift.[50]

To assess the possible application in optical thermometers, the thermometric performance was evaluated by implementing the bandwidth (FWHM) and band shift of the $^4T_2 \rightarrow {}^4A_2$ emission band of Cr^{3+} ions. Noteworthy is the fact that at 350 K, the FWHM and band centroid deviated from their temperature dependence, implying that the working temperature range was selected to be 80–350 K. The band-shift and FWHM parameters were both related to temperature and effectively fitted to polynomial formulas, with $R^2 = 0.998$ and 0.997, respectively (Fig. 7a and c). In Table S1 (ESI†), the relevant fitting parameters are presented. The determined temperature are sensitivity values for the bandwidth (d(FWHM)/dT) as a relation of temperature are exhibited in Fig. 7b, revealing the maximal rate of the band broadening was 0.337 nm K^{-1} at 208 K. The sensitivity values based on the band-shift (d($\lambda_{centroid}$)/dT) were also calculated (Fig. 7d), showing that the maximal rate of the band-shifting was 0.272 nm K^{-1} at 213 K. Furthermore, the obtained sample has better sensitivity than previously discovered
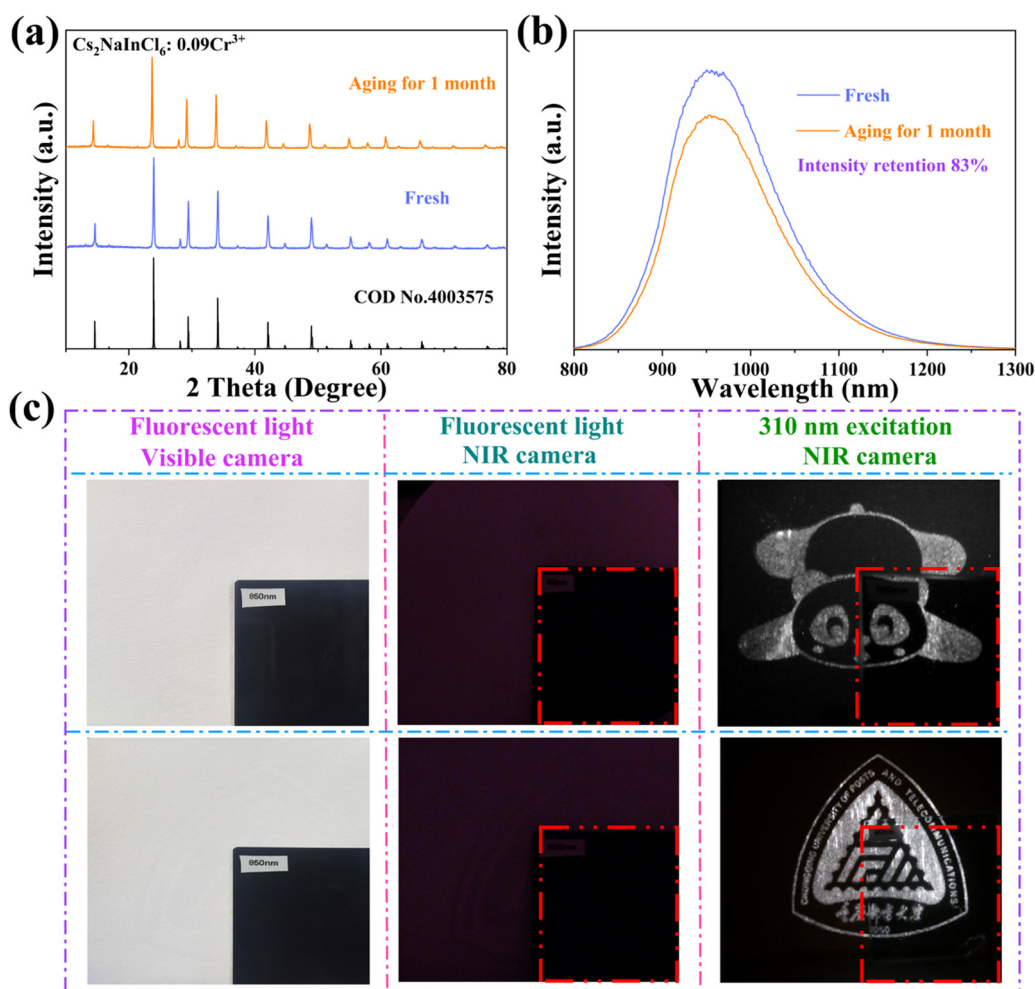

Fig. 8 (a) XRD patterns and (b) PL emission spectra of Cs$_2$NaInCl$_6$:0.09Cr^{3+} over an aging time for 1 month. (c) Photographs taken in daylight with a visible camera and in the dark with an NIR camera when the 310 nm UV excitation light is turned off and on.
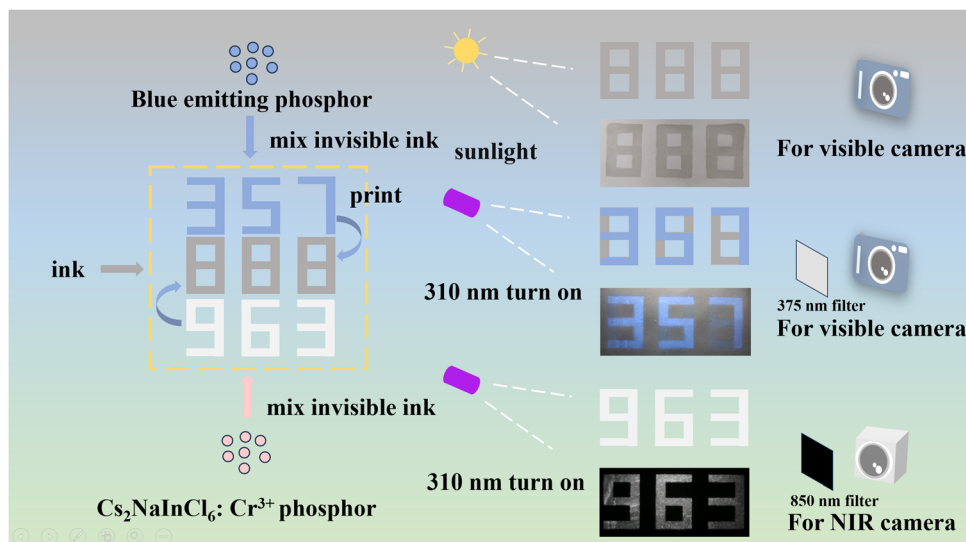
Fig. 9 Information encryption method. The "888" pattern is noticeable in daylight. Under 310 nm excitation, the visible light camera captures the light emitted by the blue phosphor, showing a "357" pattern; the near-infrared camera captures the near-infrared light emitted by $Cs_2NaInCl_6:Cr^{3+}$, showing the pattern of "963".

lanthanide-based luminous thermometers with the aid of the FWHM and emission band-shift.[51–54]

Along with the aforementioned optical properties, ensuring long-term stability in both the perovskite structure and its optical characteristics is essential for practical applications. To assess the resilience of the sample towards chemical and thermal stabilities, $Cs_2NaInCl_6:Cr^{3+}$ was aged at room temperature for one month, after which the samples were retested. The obtained results demonstrate negligible changes in XRD patterns after this duration of aging (Fig. 8a). Furthermore, even after this period, the integrated PL intensity of $Cs_2NaInCl_6:Cr^{3+}$ remained at 83% of its initial value (Fig. 8b). In addition, the thermal stability test of $Cs_2NaInCl_6:Cr^{3+}$ was performed by TGA. The TGA curve of the $Cs_2NaInCl_6:Cr^{3+}$ was measured from 25 to 800 °C (Fig. S2, ESI†). The results imply that the sample demonstrates exceptional thermal stability, as there is no weight fluctuation shift below 580 °C. Compared with organic–inorganic hybrid materials, $Cs_2NaInCl_6:Cr^{3+}$ has higher stability against high temperatures.

Eventually, the security ink based on the $Cs_2NaInCl_6:Cr^{3+}$ powder was fabricated, and a screen printing technique was further utilized to produce intricate patterns. The luminescence patterns with NIR emission are displayed in Fig. 8c. Furthermore, we designed an information encryption mode using the material in conjunction with commercial blue phosphor (Fig. 9). In visible light, the "888" pattern was displayed. Under 310 nm excitation, the "357" pattern was displayed, indicating the emanated light from the blue phosphor, which reveals the first encryption mode. Simultaneously, using the NIR camera, the "963" pattern shows a second encryption mode that is imperceptible to the human eye. The NIR optical properties of the material improve the security of the information encryption, exhibiting unique advantages in the fields of anti-counterfeiting and information encryption.

4. Conclusions

In conclusion, this work successfully synthesizes $Cs_2NaInCl_6:Cr^{3+}$ double perovskite using the solvothermal method, and its structures, optical properties, luminescence mechanism, and applications were studied. $Cs_2NaInCl_6:Cr^{3+}$ phosphors exhibit a broad range of NIR emission of 800–1300 nm upon excitation at 292 nm. The temperature-dependent PL emission spectra were analyzed to investigate the sensing sensitivity in both bandwidth and band-shift thermometry modes, achieving high sensitivity values of 0.337 nm K^{-1} for bandwidth thermometry and 0.272 nm K^{-1} for band-shift thermometry. Additionally, the material can be used to create patterns that demonstrate its potential for NIR information encryption applications.

Conflicts of interest

There are no conflicts to declare.

Acknowledgements

References

1 A. Ho-Baillie, M. Zhang, C. F. J. Lau, F.-J. Ma and S. Huang, Untapped Potentials of Inorganic Metal Halide Perovskite Solar Cells, *Joule*, 2019, **3**, 938–955.

4636 | *J. Mater. Chem. C*, 2024, **12**, 4627–4639

This journal is © The Royal Society of Chemistry 2024

2 X.-K. Liu, W. Xu, S. Bai, Y. Jin, J. Wang, R. H. Friend and F. Gao, Metal halide perovskites for light-emitting diodes, *Nat. Mater.*, 2021, **20**, 10–21.

3 H. Wang, S. Li, X. Liu, Z. Shi, X. Fang and J. He, Low-Dimensional Metal Halide Perovskite Photodetectors, *Adv. Mater.*, 2021, **33**, 2003309.

4 W. Xiang, S. (Frank) Liu and W. Tress, A review on the stability of inorganic metal halide perovskites: challenges and opportunities for stable solar cells, *Energy Environ. Sci.*, 2021, **14**, 2090–2113.

5 B. Zhang, L. Goldoni, J. Zito, Z. Dang, G. Almeida, F. Zaccaria, J. De Wit, I. Infante, L. De Trizio and L. Manna, Alkyl Phosphonic Acids Deliver $CsPbBr_3$ Nanocrystals with High Photoluminescence Quantum Yield and Truncated Octahedron Shape, *Chem. Mater.*, 2019, **31**, 9140–9147.

6 S. Shi, Y. Wang, S. Zeng, Y. Cui and Y. Xiao, Surface Regulation of $CsPbBr_3$ Quantum Dots for Standard Blue-Emission with Boosted PLQY, *Adv. Opt. Mater.*, 2020, **8**, 2000167.

7 Z. Xiao, Z. Song and Y. Yan, From Lead Halide Perovskites to Lead-Free Metal Halide Perovskites and Perovskite Derivatives, *Adv. Mater.*, 2019, **31**, 1803792.

8 L. Chu, W. Ahmad, W. Liu, J. Yang, R. Zhang, Y. Sun, J. Yang and X. Li, Lead-Free Halide Double Perovskite Materials: A New Superstar Toward Green and Stable Optoelectronic Applications, *Nano-Micro Lett.*, 2019, **11**, 16.

9 Y. Zhu, G. Pan, J. Zhao, K. Liu, W. Xue, Y. Wang, W. You, H. Gao, W. Xu and Y. Mao, High-Efficiency Dual-Mode Polychromatic Emission of Rare-Earth-Based Double Perovskite with Low Phonon Energy toward High-Level Anti-Counterfeiting and Information Encryption, *Adv. Opt. Mater.*, 2023, **11**, 2202019.

10 F. Igbari, Z. Wang and L. Liao, Progress of Lead-Free Halide Double Perovskites, *Adv. Energy Mater.*, 2019, **9**, 1803150.

11 J. Luo, X. Wang, S. Li, J. Liu, Y. Guo, G. Niu, L. Yao, Y. Fu, L. Gao, Q. Dong, C. Zhao, M. Leng, F. Ma, W. Liang, L. Wang, S. Jin, J. Han, L. Zhang, J. Etheridge, J. Wang, Y. Yan, E. H. Sargent and J. Tang, Efficient and stable emission of warm-white light from lead-free halide double perovskites, *Nature*, 2018, **563**, 541–545.

12 F. Ji, J. Klarbring, F. Wang, W. Ning, L. Wang, C. Yin, J. S. M. Figueroa, C. K. Christensen, M. Etter, T. Ederth, L. Sun, S. I. Simak, I. A. Abrikosov and F. Gao, Lead-Free Halide Double Perovskite $Cs_2AgBiBr_6$ with Decreased Band Gap, *Angew. Chem.*, 2020, **132**, 15303–15306.

13 F. Locardi, M. Cirignano, D. Baranov, Z. Dang, M. Prato, F. Drago, M. Ferretti, V. Pinchetti, M. Fanciulli, S. Brovelli, L. De Trizio and L. Manna, Colloidal Synthesis of Double Perovskite $Cs_2AgInCl_6$ and Mn-Doped $Cs_2AgInCl_6$ Nanocrystals, *J. Am. Chem. Soc.*, 2018, **140**, 12989–12995.

14 B. Zhou, Z. Liu, S. Fang, H. Zhong, B. Tian, Y. Wang, H. Li, H. Hu and Y. Shi, Efficient White Photoluminescence from Self-Trapped Excitons in Sb^{3+}/Bi^{3+}-Codoped $Cs_2NaInCl_6$ Double Perovskites with Tunable Dual-Emission, *ACS Energy Lett.*, 2021, **6**, 3343–3351.

15 R. Zeng, L. Zhang, Y. Xue, B. Ke, Z. Zhao, D. Huang, Q. Wei, W. Zhou and B. Zou, Highly Efficient Blue Emission from Self-Trapped Excitons in Stable Sb^{3+}-Doped $Cs_2NaInCl_6$ Double Perovskites, *J. Phys. Chem. Lett.*, 2020, **11**, 2053–2061.

16 J. Nie, B. Zhou, S. Fang, H. Zhong, H. Li and Y. Shi, Efficient Multicolor and White Photoluminescence in Erbium- and Holmium-Incorporated $Cs_2NaInCl_6$:Sb^{3+} Double Perovskites, *Chem. Mater.*, 2022, **34**, 6288–6295.

17 D. Liu, G. Li, P. Dang, Q. Zhang, Y. Wei, H. Lian, M. Shang, C. C. Lin and J. Lin, Simultaneous Broadening and Enhancement of Cr^{3+} Photoluminescence in $LiIn_2SbO_6$ by Chemical Unit Cosubstitution: Night-Vision and Near-Infrared Spectroscopy Detection Applications, *Angew. Chem., Int. Ed.*, 2021, **60**, 14644–14649.

18 W. Zhao, L. Li, Z. Wu, Y. Wang, Z. Cao, F. Ling, S. Jiang, G. Xiang, X. Zhou and Y. Hua, Bifunctional near-infrared-emitting phosphors of chromium(III)-activated antimonates for NIR light-emitting diodes and low-temperature thermometry, *J. Alloys Compd.*, 2023, **965**, 171370.

19 J. Zhang, D. Huang, C. Huang, S. Liang and H. Zhu, Investigation on the Luminescent Property and Application of $In_2BP_3O_{12}$: Cr^{3+} Broadband Near-Infrared Phosphor, *Acta Chim. Sin.*, 2022, **80**, 453–459.

20 X. Wu, S. Zhan, J. Han and Y. Liu, Nanoscale Ultrasensitive Temperature Sensing Based on Upconversion Nanoparticles with Lattice Self-Adaptation, *Nano Lett.*, 2021, **21**, 272–278.

21 G. B. Nair, A. Kumar, S. J. Dhoble and H. C. Swart, Synergistic effect from the dual oxidation states of europium in the color-tuning of $Ca_3Mg_3(PO_4)_4$: Eu^{2+}, Eu^{3+} thermometric phosphor, *Mater. Res. Bull.*, 2020, **122**, 110644.

22 Q. Wang, M. Liao, Q. Lin, M. Xiong, Z. Mu and F. Wu, A review on fluorescence intensity ratio thermometer based on rare-earth and transition metal ions doped inorganic luminescent materials, *J. Alloys Compd.*, 2021, **850**, 156744.

23 Q. Wang, Z. Liang, J. Luo, Y. Yang, Z. Mu, X. Zhang, H. Dong and F. Wu, Ratiometric optical thermometer with high sensitivity based on dual far-red emission of Cr^{3+} in $Sr_2MgAl_{22}O_{36}$, *Ceram. Int.*, 2020, **46**, 5008–5014.

24 Z. Wu, L. Li, Y. Wang, F. Ling, Z. Cao, S. Jiang, G. Xiang, X. Zhou, Y. Hua and J. S. Yu, High-sensitivity luminescent thermometer based on Mn^{4+}/Sm^{3+} dual-emission centers in double-perovskite tellurate, *Ceram. Int.*, 2022, **48**, 27664–27671.

25 X. Zhang, H. Zheng, J. Hu, F. Lu, X. Peng, R. Wei, F. Hu and H. Guo, Enhanced up-conversion luminescence and temperature sensing property of Ba Sr Lu_4O_9:Tm^{3+}/Yb^{3+} phosphors, *Ceram. Int.*, 2021, **47**, 32290–32296.

26 C. D. S. Brites, P. P. Lima, N. J. O. Silva, A. Millán, V. S. Amaral, F. Palacio and L. D. Carlos, A Luminescent Molecular Thermometer for Long-Term Absolute Temperature Measurements at the Nanoscale, *Adv. Mater.*, 2010, **22**, 4499–4504.

27 R. M. Diaz-Rodriguez, D. A. Gálico, D. Chartrand, E. A. Suturina and M. Murugesu, Toward Opto-Structural Correlation to Investigate Luminescence Thermometry in an Organometallic Eu(II) Complex, *J. Am. Chem. Soc.*, 2022, **144**, 912–921.

This journal is © The Royal Society of Chemistry 2024

J. Mater. Chem. C, 2024, **12**, 4627–4639 | **4637**

28 U. Rocha, C. Jacinto Da Silva, W. Ferreira Silva, I. Guedes, A. Benayas, L. Martínez Maestro, M. Acosta Elias, E. Bovero, F. C. J. M. Van Veggel, J. A. García Solé and D. Jaque, Subtissue Thermal Sensing Based on Neodymium-Doped LaF$_3$ Nanoparticles, *ACS Nano*, 2013, **7**, 1188–1199.

29 D. K. Amarasinghe and F. A. Rabuffetti, Bandshift Luminescence Thermometry Using Mn^{4+}: Na$_4$Mg(WO$_4$)$_3$ Phosphors, *Chem. Mater.*, 2019, **31**, 10197–10204.

30 J. Hafner, *Ab-initio* simulations of materials using VASP: Density-functional theory and beyond, *J. Comput. Chem.*, 2008, **29**, 2044–2078.

31 G. Kresse and J. Furthmüller, Efficient iterative schemes for *ab initio* total-energy calculations using a plane-wave basis set, *Phys. Rev. B: Condens. Matter Mater. Phys.*, 1996, **54**, 11169–11186.

32 A. Zhang, Y. Liu, G. Liu and Z. Xia, Dopant and Compositional Modulation Triggered Broadband and Tunable Near-Infrared Emission in Cs$_2$Ag$_{1-x}$Na$_x$ InCl$_6$: Cr^{3+} Nanocrystals, *Chem. Mater.*, 2022, **34**, 3006–3012.

33 N. Mironova-Ulmane, M. G. Brik, J. Grube, G. Krieke, M. Kemere, A. Antuzevics, E. Gabrusenoks, V. Skvortsova, E. Elsts, A. Sarakovskis, M. Piasecki and A. I. Popov, EPR, optical and thermometric studies of Cr^{3+} ions in the α-Al$_2$O$_3$ synthetic single crystal, *Opt. Mater.*, 2022, **132**, 112859.

34 D. Chen, X. Zhang, J. Wei, L. Zhou, P. Chen, Q. Pang and J. Z. Zhang, Simultaneous enhancement of near infrared luminescence and stability of Cs$_2$AgInCl$_6$: Cr^{3+} double perovskite single crystals enabled by a Yb^{3+} dopant, *Inorg. Chem. Front.*, 2022, **9**, 4695–4704.

35 F.-J. Meng and X.-M. Guo, Tuning the oxygen defects and Fermi levels via In^{3+} doping in SnO$_2$-In$_2$O$_3$ nanocomposite for efficient CO detection, *Sens. Actuators, B*, 2022, **357**, 131412.

36 M. A. Muñoz-Márquez, M. Zarrabeitia, E. Castillo-Martínez, A. Eguía-Barrio, T. Rojo and M. Casas-Cabanas, Composition and Evolution of the Solid-Electrolyte Interphase in Na$_2$Ti$_3$O$_7$ Electrodes for Na-Ion Batteries: XPS and Auger Parameter Analysis, *ACS Appl. Mater. Interfaces*, 2015, **7**, 7801–7808.

37 W. Zhou, J. Luo, J. Fan, H. Pan, S. Zeng, L. Zhou, Q. Pang and X. Zhang, Luminescent properties and LED Application of Broadband Near-Infrared Emitting NaInGe$_2$O$_6$:Cr^{3+} phosphors, *Ceram. Int.*, 2021, **47**, 25343–25349.

38 J. Zhou, X. Rong, P. Zhang, M. S. Molokeev, P. Wei, Q. Liu, X. Zhang and Z. Xia, Manipulation of Bi^{3+}/In^{3+} Transmutation and Mn^{2+}-Doping Effect on the Structure and Optical Properties of Double Perovskite Cs$_2$NaBi$_{1-x}$ In$_x$Cl$_6$, *Adv. Opt. Mater.*, 2019, **7**, 1801435.

39 K. Indumathi, S. Tamilselvan, L. Rajasekaran, A. D. J. David, G. S. Muhammad, G. Ramalingam and M. Biruntha, Structural and optical properties of Eu^{3+} doped Sr$_3$Gd[PO$_4$]$_3$ phosphor white-LED application, *Mater. Lett.*, 2022, **309**, 131371.

40 Z. Shao, X. Zhou, L. Li, Y. Wang, F. Ling, C. Jing, X. Tang and Z. Cao, Broadband near-infrared double-perovskite phosphor Sr$_2$ScTaO$_6$:Cr^{3+},Yb^{3+} for NIR pc-LED applications, *Ceram. Int.*, 2023, S0272884223021995.

41 C.-H. Lu, Y.-T. Tsai, T.-L. Tsai, T.-S. Chan, X. Zhang and C. C. Lin, Cr^{3+}-Sphere Effect on the Whitlockite-Type NIR Phosphor Sr$_9$Sc(PO$_4$)$_7$ with High Heat Dissipation for Digital Medical Applications, *Inorg. Chem.*, 2022, **61**, 2530–2537.

42 Q. Wang, S. Wang, T. Tan, J. Wang, R. Pang, D. Li, C. Li and H. Zhang, Efficient Cr^{3+}-activated NaInP$_2$O$_7$ phosphor for broadband near-infrared LED applications, *Inorg. Chem. Front.*, 2022, **9**, 3692–3701.

43 T. Yu, H. Sheng, S. Chen, J. Yuan, T. Deng, M. Wu, Y. Guo and Q. Zeng, A broadband near-infrared Sc$_{1-x}$(PO$_4$)$_3$: X Cr^{3+} phosphor with enhanced thermal stability and quantum yield by Yb^{3+} codoping, *J. Am. Ceram. Soc.*, 2022, **105**, 3403–3417.

44 S. Miao, Y. Liang, Y. Zhang, D. Chen and X. Wang, Blue LED-Pumped Broadband Short-Wave Infrared Emitter Based on LiMgPO$_4$: Cr^{3+}, Ni^{2+} Phosphor, *Adv. Mater. Technol.*, 2022, **7**, 2200320.

45 F. Zhao, Z. Song and Q. Liu, Novel Cr^{3+}-activated far-red emitting phosphors with β-Ca$_3$(PO$_4$)$_2$-type structure for indoor plant cultivation, *Int. J. Miner., Metall. Mater.*, 2022, **29**, 1286–1294.

46 F. Y. Zhao, H. Cai, S. Y. Zhang, Z. Song and Q. L. Liu, Octahedron-dependent near-infrared luminescence in Cr^{3+}-activated phosphors, *Mater. Today Chem.*, 2022, **23**, 100704.

47 X. Feng, L. Lin, R. Duan, J. Qiu and S. Zhou, Transition metal ion activated near-infrared luminescent materials, *Prog. Mater. Sci.*, 2022, **129**, 100973.

48 B. Malysa, A. Meijerink and T. Jüstel, Temperature dependent photoluminescence of Cr^{3+} doped Sr$_8$MgLa(PO$_4$)$_7$, *Opt. Mater.*, 2018, **85**, 341–348.

49 S. Miao, Y. Liang, Y. Zhang, D. Chen, S. Yan, J. Liu and X.-J. Wang, Spectrally tunable and thermally stable near-infrared luminescence in Na$_3$Sc$_2$(PO$_4$)$_3$:Cr^{3+} phosphors by Ga^{3+} co-doping for light-emitting diodes, *J. Mater. Chem. C*, 2022, **10**, 994–1002.

50 F. Zhao, Z. Song, J. Zhao and Q. Liu, Double perovskite Cs$_2$AgInCl$_6$:Cr^{3+}: broadband and near-infrared luminescent materials, *Inorg. Chem. Front.*, 2019, **6**, 3621–3628.

51 A. Ćirić, S. Stojadinović and M. D. Dramićanin, Time-integrated luminescence thermometry of Eu^{3+} and Dy^{3+} doped YVO$_4$, *Sens. Actuators, Phys.*, 2019, **295**, 450–455.

52 J. Periša, Z. Ristić, W. Piotrowski, Ž. Antić, L. Marciniak and M. D. Dramićanin, All near-infrared multiparametric luminescence thermometry using Er^{3+}, Yb^{3+}-doped YAG nanoparticles, *RSC Adv.*, 2021, **11**, 15933–15942.

53 T. Zheng, M. Runowski, N. Stopikowska, M. Skwierczyńska, S. Lis, P. Du and L. Luo, Dual-center thermochromic Bi$_2$MoO$_6$:Yb^{3+},Er^{3+},Tm^{3+} phosphors for ultrasensitive luminescence thermometry, *J. Alloys Compd.*, 2022, **890**, 161830.

54 T. Zheng, M. Sójka, M. Runowski, P. Woźny, S. Lis and E. Zych, Tm^{2+} Activated SrB$_4$O$_7$ Bifunctional Sensor of Temperature and Pressure—Highly Sensitive, Multi-Parameter Luminescence Thermometry and Manometry, *Adv. Opt. Mater.*, 2021, **9**, 2101507.

4638 | *J. Mater. Chem. C*, 2024, **12**, 4627–4639

This journal is © The Royal Society of Chemistry 2024

55 J. Zhang, W. Zhao, X. Zhang, Y. Li, W. Zhang, H. Wen and J. Zhong, Ultra-broadband near-infrared emission in the double-perovskite Ca_2InTaO_6:Cr^{3+} phosphor for light-emitting-diode applications, *J. Lumin.*, 2023, **255**, 119581.

56 H. Zhang, C. Li, J. Zhong, J. Wen and W. Zhao, Thermally Robust Broadband Near-Infrared Luminescence in the $NaGaP_2O_7$:Cr^{3+} Phosphor, *ACS Appl. Opt. Mater.*, 2023, **1**, 85–93.

57 J. Zhong, C. Li, W. Zhao, S. You and J. Brgoch, Accessing High-Power Near-Infrared Spectroscopy Using Cr^{3+}-Substituted Metal Phosphate Phosphors, *Chem. Mater.*, 2022, **34**, 337–344.

58 F. Zhao, H. Cai, Z. Song and Q. Liu, Structural Confinement for Cr^{3+} Activators toward Efficient Near-Infrared Phosphors with Suppressed Concentration Quenching, *Chem. Mater.*, 2021, **33**, 3621–3630.

This journal is © The Royal Society of Chemistry 2024

J. Mater. Chem. C, 2024, **12**, 4627–4639 | **4639**